$LiFePO_4$ spray drying scale-up and carbon-cage for improved cyclability

Marco G. Rigamonti[a], Marc Chavalle[b], He Li[a], Philippe Antitomaso[c], Lida Hadidi[c], Marta Stucchi[d], Federico Galli[a], Hayat Khan[a], Mickael Dollé[c], Daria Camilla Boffito[a], Gregory S. Patience[a,*]

[a]*Department of Chemical Engineering, Polytechnique Montréal, C.P. 6079, Succ. CV Montréal, H3C 3A7 Québec, Canada.*
[b]*Laboratory of Soft Matter Science and Engineering, École supérieure de physique et de chimie industrielles de la Ville de Paris, 10 rue Vauquelin, 75005 Paris, France.*
[c]*Laboratory Chemistry and Electrochemistry of Solids, Université de Montréal, 2900 boul. Édouard-Montpetit, H3T 1J4 Montréal, Québec, Canada.*
[d]*Dipartimento di Chimica, Università degli Studi di Milano, via Golgi 19, 20133 Milano, Italy.*

Abstract

The growing market for electrical vehicles requires inexpensive, long-lasting batteries. $LiFePO_4$ (LFP) melt-synthesized from ore concentrate fits this role, but the manufacturing process requires additional steps that includes grinding large ingots into a nanoparticle suspension followed by a dessication step. Spray drying, rather than tray drying, creates a mesoporous powder that enhances wettability. Adding lactose and high-M_w polyvinyl alcohol (PVA) to the suspension of nanostructures followed by pyrolysis, creates a carbon-cage that interconnects the cathode nanoparticles, imparting better capacity ($LiFePO_4$/C: 161 mA h g^{-1} at 0.1C), discharge rate (flat plateau, 145 mA h g^{-1} at 5C), and cyclablity (91 % capacity retention after 750 cycles at 1C). Particle size affects battery stability; PVA increases the suspension's viscosity and alters the powder morphology, from spherical to hollow particles. A model describes the non-Newtonian suspension's rheology changing: shear, temperature, LFP and PVA loading. Carbon precursors prevent the nanoparticles from sintering during calcination but lactose gasifies 50 % of the carbon, according to the chemical and allotropic composition measurements (CS analyzer, XPS, and Raman). The carbon-cage imparts microporosity and we correlate the SEM and TEM powder's morphology with N_2 physisorption porosimetry. Ultrasonication of the suspension fragments the PVA chain, which is detrimental to the final cathode performance.

Keywords: $LiFePO_4$/C cathode material, nanoparticle, spray drying, pyrolysis, carbon-cage, electrochemical test

1. Introduction

Lithium-ion batteries power our life: cellphones and computers count in the billions of units, and a new technology sector aims to scale-up batteries for the automotive industry and for stationary energy storage systems.[1] For this strategic vision, batteries with high-efficiency, long-life, and low-cost are the best choice to facilitate the transition from fossil fuel vehicles to electric. This vision also requires electric storage units to create a reliable and flexible grid system to smooth-out a fluctuating supply from renewable sources.[2] The cathode represents the bottle-neck of this technology as its capacity is an order of magnitude lower than the graphite anode. The lithium-sulfur cell with a glass solid-state electrolyte promises to lead the next generation of batteries, but despite their outstanding cycle life (above 15000), and improved capacity (reaching 500 mA h g^{-1}), cost and scalability are potential deterrents for adoption.[3] Carbon nanotubes (CN)

*Corresponding author
Email address: gregory-s.patience@polymtl.ca (Gregory S. Patience)

demonstrate high power output and excellent cycling performance in a $ZnFe_2O_4$−C/$LiFePO_4$−CNT battery, but only at a laboratory scale (10000 cycles at 10C, retained 85 % of the initial capacity).[4] $LiCoO_2$, at 273 mA h g^{-1}, is currently the cathode of choice for electric vehicles, but is costly and has safety and environmental issues.[5] $LiFePO_4$ (LFP) has a lower capacity (170 mA h g^{-1}) but it costs less, is thermally stable, and its precursors are environmentally benign.[6, 7] LFP electrical performance is optimal at a particle size of 200 nm,[8] with a carbon black[9] or metal oxides[10, 11] coating since $LiFePO_4$ has a low Li^+ diffusivity in the olivine crystalline matrix and a low electrical conductivity. Melt-cast processes produce pure, crystalline materials with lower-grade purity precursors at 40 % the cost.[12, 13] In our process, a furnace heats the precursors to above 1100 °C and after reaction, the molten liquid is poured into molds to form ingots. Subsequently, a jaw crusher and a roller grinder produce granules then a powder 25 µm in diameter. A wet media mill reduces the particle size to 200 nm in water. Removing solvent from nanoparticle suspension requires the same diligence as drying pharmaceutical ingredients. The cathode material oxidizes, sinters into chunks, and Li_3PO_4 segregates when drying in a furnace. Spray drying preserves the original chemical and morphological properties because of the short contact time of the material in contact with the hot air (10 s to 60 s), delivering fine monodispersed granules. In addition, spray drying is already an established technology in the catalyst, pharmaceutical and food industries because of they are easy to scale-up, high productivity and low operating costs. In this paper, we demonstrate the scale-up feasibility of spray drying melt-synthesized $LiFePO_4$ and inexpensive organic precursors that self-assemble into a carbon cage. This increases the cathode cyclability and discharge rate similarly to CN, but at a higher productivity-rate and lower cost of carbon-precursors (250 fold with respect to CN).[14] The organic precursors are mixed with the suspension and pass through a two-fluid compressed-air nozzle atomizer feeding into the drying chamber where hot air evaporates the water and microscopic droplets form (up to 100 µm), The suspended nanoparticles (primary particles, 0.07 µm to 0.2 µm) agglomerate into porous, spherical or doughnut-shaped, secondary particles (5 µm to 50 µm). The resulting porous powder is then calcined to pyrolyze the organic precursors to semi-graphitic carbon, which enhances the electrical conductivity of the material. Finally, we evaluated the electrochemical quality of the LFP/C cathode in coin cells.

2. Experimental section

We reported our reagents and characterization techniques under Electronic Supplementary Information (ESI).

2.1. Nanoparticle suspension preparation

An induction furnace at 1100 °C melted the precursors and synthesized LFP in a graphite crucible with a capacity of 50 kg The feed materials were: LiH_2PO_4, P_2O_5, Li_2CO_3 and iron ore concentrate (>99 % Fe_2O_3 with SiO_2 impurity) with a Li/Fe/P: 1.03/1/1.03 stoichiometry,[15, 16, 17] and we cast the melt into 200 mm ingots.[18] LFP is the dry solid fraction of our feed material, constisting of 97.8 % $LiFePO_4$ and 2.2 % γ-Li_3PO_4 (±0.4 % $CI^{95\,\%}_{n=6}$, by AAS and XRD; 95 % confidence interval estimate, with a two-tail t-test for a sample number n).

A Pulverisette 1 model II, Fritzch jaw crusher ground the ingots to 1 mm to 3 mm gravel, processing 13 kg h^{-1} of material. A roller grinder (MPE 6F granulizer, Chicago) further reduced the particle size to a $d_{v,50}$ of 27 µm and $d_{v,99}$ of 200 µm; treating 2 kg h^{-1} of material at a 10 % feed rate. A wet media mill (NETZSCH - LMZ 4) ground the powder,

equipped with a 0.1 mm mesh filter and loaded with 3.2 L of 0.68 mm yttria-stabilized zirconia beads, which filled 75 % of the total volume of the grinding chamber. Pilot and commercial grinding chambers are made of ceramic rather than stainless steel to minimize iron contamination. We filled the apparatus with 25 L of deionized water and loaded 25 kg of LFP, with a 0.008 mass ratio of Tween-20 surfactant in the mixing tank. We scaled-up the process based on our previous laboratory experience and added LFP progressively at a rate slow enough to avoid plugging the mesh filters ($20\,\mathrm{kg\,h^{-1}}$).[19] A cooling system pumped water at 15 °C around the grinding chamber and mixing tank (ESI Figure 1S). We sampled the slurry at the outlet of the grinding chamber every 15 min and immediately analyzed by laser scattering to avoid agglomeration. We operated the wet media mill until the particle size distribution (PSD) median reached 200 nm.

2.2. Spray drying

Despite the Tween-20 surfactant, the suspended primary particles tended to settle when stored for weeks. A mechanical mixer homogenized the slurry periodically and an aliquot of material was weighed and ultrasonicated for 15 min before each experiment to de-agglomerate the nanoparticles.[20] For standard feed materials, we added binders (lactose or polyvinyl alcohol solution, 1 % to 7 %) and mechanically stirred the suspension for an additional 15 min. For ultrasonicated slurries (US), we added the binders while stirring and ultrasonicating for 15 min. We spray dried the feed material with a GEA Niro Mobile Minor$^{\mathrm{TM}}$-PSR pilot-scale spray dryer (0.8 m I.D. x 0.8 m height / 60° cone chamber Figure 1). An 11 kW electrical coil heated $90\,\mathrm{kg\,h^{-1}}$ of drying air to 350(2) °C, which flowed co-currently with the spray, leaving the bottom of the chamber at 125(2) °C. We chose a two-fluid nozzle, with 0.7 mm I.D. for the liquid and 3.1 mm I.D. 5.0 mm O.D. for the atomizing air, based on laboratory-scale tests of flowability of LFP suspensions through a bore restriction (ESI).[21, 22] Compressed air at 0.25 MPa to 0.40 MPa fed the nozzle while a peristaltic pump fed the suspension at flow rates between $130\,\mathrm{mL\,min^{-1}}$ to $180\,\mathrm{mL\,min^{-1}}$, creating a fine mist. A cyclone separated the resulting powder, with a 50 % cut-off efficiency for 0.7 µm, $1600\,\mathrm{kg\,m^{-3}}$ secondary particles. Before feeding the suspension, we reached thermal steady state with an equivalent volumetric flow of water (up to $90\,\mathrm{mL\,min^{-1}}$) during 2 h.

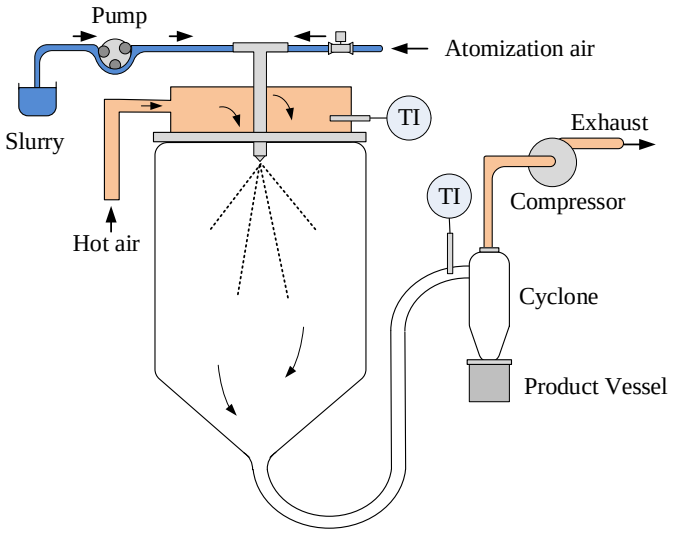

Figure 1: GEA Mobile minor spray dryer setup. The recovery yield averaged 80 %: 10 % of the material coats the chamber and another 10 % escapes the cyclone.

2.3. Calcination and electrochemical tests

We loaded 2 g of spray dried powder into an alumina crucible and inserted it in a tube furnace flushed with a N_2 atmosphere. We let the powder outgas at 100 °C for 2 h and then increased the temperature to 700 °C for 2 h to calcine the material. The electrode of carbon coated LFP was prepared by mixing the pyrolyzed active material ($LiFePO_4$/C, 500 mg), with carbon black C65 as conductive additive, and polyvinylidene fluoride (PVDF) at a weight ratio of 84:9:7 in N-methyl-2-pyrrolidone (NMP) solvent. The mixture was then shaken in a Turbula 3D mixer for 20 min, and homogenized in a tube roller overnight with 5 mm by 6 mm cylindrical beads. The uniform slurry was spread onto a piece of aluminum foil current collector using the doctor blade technique. The electrode dried in a vacuum oven at 80 °C overnight. Disc-shaped electrodes with a loading of 1.8(1) mg cm^{-2}, and a thickness of 24 µm, were cut and assembled in coin cells (2032) in an argon filled glove box. A lithium metal foil was used as the negative electrode, $LiFePO_4$/C as the positive one, Celgard 2400 as the separator, and 1 M $LiPF_6$ in ethylene carbonate-dimethyl carbonate (weight ratio of 1:2) solvent as the electrolyte. The electrochemical tests were performed on the cells at 30 °C on a Arbin BT2000 electrochemical station with cut-off voltages of 2.2 V and 4.0 V vs Li^+/Li at a 0.1C-rate for galvanostatic cycling and at 0.1C to 10C-rates to determine the power performance.

3. Results and discussion

3.1. LFP characterization and elemental analysis

Spray drying atomizes the suspension into droplets that have a short residence time in the chamber (14 s). As long as the droplets contain any(water, the water evaporates below its boiling point, and by the time the powder become bone-dry, the spray dryer effluent temperature has dropped to 125 °C, due to the latent heat of vaporization. This phenomena minimizes any oxidation or chemical alteration of the feed material, even when spray drying up to an inlet temperature of 350 °C, as long the outlet temperature remains below such transitions.[22] In comparison, drying the slurry in air on a hot plate at 180 °C, partially overoxidizes the material to Fe^{3+}: $Li_3Fe_2(PO_4)_3$ and Fe_2P that have characteristic XRD peaks at 27.5° and 41.0° 2θ.[23, 24] Instead, the only additional crystalline phase of spray dried LFP is a constituent of the formulation (γ-Li_3PO_4), because of its stoichiometric deficiency of iron, which beneficial for the final battery formulation.[15] While we add an excess of phosphorus, some volatilizes in the spray dryer and somer reacts with the graphite crucible forming Fe_2P, which remains embedded in the crucible pores. The synthesis yields $LiFePO_4$ and the excess of lithium and phosphate recombine forming γ-Li_3PO_4 (Figure 2a).

Solid-state reactions form γ-Li_3PO_4 (COD ref: 901-282), at a phase transition temperature of 1170 °C, with improved ionic conductivity vs. the β-Li_3PO_4 (COD ref: 901-2500), synthesized by wet chemical reaction (3×10^{-7} S cm^{-1} vs. 4×10^{-8} S cm^{-1}).[25] Milling in water and drying dissolves and recrystallizes this phase. However, Li_3PO_4 is poorly soluble in water (0.4 g L^{-1} at 20 °C). In a slurry containing 50 % LFP, there are 11 g L^{-1} of Li_3PO_4. Only 4 % of Li_3PO_4 is in solution, the remaining is embedded in the solid matrix of LFP as γ-Li_3PO_4. The Rietveld refinement estimates γ-Li_3PO_4 at 1.4(3) % for our samples (ESI Table 1S). However, the calcined samples without carbon precursors diffract more (1.9 % γ-Li_3PO_4), while spray dried samples or calcined samples with a carbon precursor diffract less (1.2(1) %

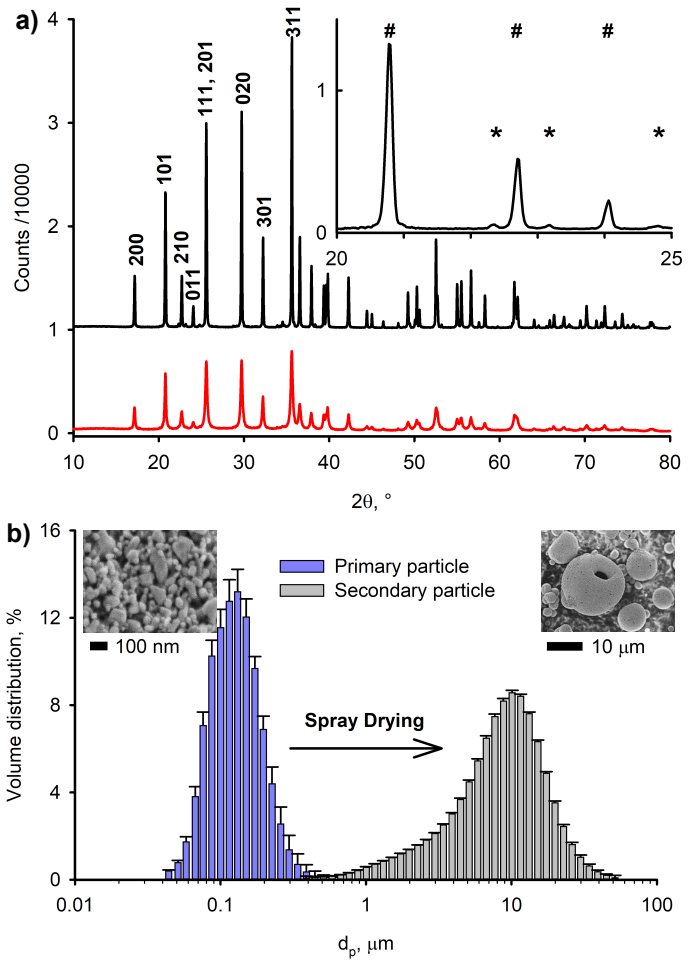

Figure 2: a) The spray dried LFP (red, bottom) presents broad peaks; calcination improves crystallinity and the sample diffracts three times more (black, top). Top-right insert: # $LiFePO_4$, * Li_3PO_4. b) The primary particles suspended in water agglomerate to secondary particles during spray drying. The resulting powder is homogeneous but sampling the suspension induces changes and increases the experimental variance. Error bars for a $CI_{n=5}^{95\,\%}$.

γ-Li_3PO_4), despite starting from the same feed material (2.2 % Li_3PO_4 by AAS). The carbon coating is a few nanometers thick and does not suppress the XRD signal from the bulk LFP (in our conditions the penetration length ranges from 30 µm to 200 µm along the 2θ angle). This indicates that, after spray drying, part of the Li_3PO_4 is amorphous or coats the surface into mono-atomic layers. Calcination sinters Li_3PO_4 and the structure becomes more crystalline. While carbon precursors coat the LFP surface, and the resulting carbon layer introduces a mass transfer resistance that limits crystal growth and sintering for both $LiFePO_4$ and γ-Li_3PO_4 on the one hand, on the other hand, the Scherrer equation calculates 30 % smaller crystallite size after calcination due to instrument resolution for this trace compound (as Li_3PO_4 is unlikely to sublime as since its melting point is 1206 °C, ESI Table 1S). The $LiFePO_4$ average crystallite size, after spray drying, is invariant with respect to lactose or PVA concentration (27 nm by Scherrer equation from profile fitting and shape factor: 0.9), but it is a function of the LFP's melt synthesis conditions. PSD laser scattering, SEM and TEM morphology confirm an average primary particle size of 80 nm by number distribution, which indicates that several crystal grains constitute the milled primary particles.[26] Calcination of the spray dried powders induce sintering and improve crystallinity also for the $LiFePO_4$ phase. The absence of carbon precursors (neat LFP) sinters the primary particles together forming 220 nm crystallites. Lactose hinders sintering and limits crystallites growth to 80 nm (XRD, SEM). From AAS we converted the

Table 1: Spray dried powders from LFP suspensions with additives in water—all slurries include the Tween-20 surfactant. PSD: secondary particle size mode and (distribution at one standard deviation). Carbon: total carbon relative to a bone dry LFP powder ($CI^{95\,\%}_{n=3}$). S_a: specific surface area ($CI^{95\,\%}_{n=3}$), V_{pore}: pore volume ($CI^{95\,\%}_{n=3}$<0.01 cm^3 g^{-1}) and porosity φ. "Py": pyrolyzed powders. "US": ultrasonicated suspension.

Sample	ω_i LFP + additive g_i/g_{total}%	PSD µm	carbon g_C/g_{LFP}%	S_a m^2 g^{-1}	V_{pore} cm^3 g^{-1}	φ %
LFP-neat	52 % + none	11(10)	0.36(1) %	28.1(8)	0.27	49 %
LFP-neat-Py	52 % + none	11(8)	0.1 %	2.9(2)	0.06	17 %
LFP-L	48 % + 7 % lactose	8(6)	5.9 %	21.6	0.19	40 %
LFP-L-Py	48 % + 7 % lactose	8(4)	3.1 %	28.9	0.20	42 %
LFP-LP	45 % + 5 % lactose, 0.45 % PVA	12(20)	5.20(9) %	19.4	0.22	43 %
LFP-LP-Py	45 % + 5 % lactose, 0.45 % PVA	12(5)	2.9 %	32.3	0.23	45 %
LFP-LPU	45 % + 5 % lactose, 0.45 % PVA, US	11(8)	5.1 %	19.9	0.19	41 %
LFP-LPU-Py	45 % + 5 % lactose, 0.45 % PVA, US	11(8)	2.9 %	26.0	0.21	43 %

measured concentrations to molar ratio between the two ions (on average Li^+/Fe^{3+} = 1.09). We assumed the excess lithium to form Li_3PO_4 (as the only other component we detected on XRD). This corresponds to 0.03 mol of Li_3PO_4 per mole of $LiFePO_4$, and in terms of mass fraction: 97.8 % $LiFePO_4$ and 2.2 % Li_3PO_4 (±0.4 % $CI^{95\,\%}_{n=6}$). AAS and XRD measurements indicate either that the spray dried material suffers from a depletion in the iron content at some point during the process or an unintentional overload of lithium phosphate during the re-melt synthesis.

3.2. Particle size and powder morphology

The primary particles have an arithmetic mean $D_{4,3}$ diameter of 130(60) nm, with a $d_{v,10}$, $d_{v,50}$, $d_{v,90}$ of 70 nm, 120 nm and 190 nm. However, laser scattering fails to measure particles smaller than 30 nm, which are present (SEM, TEM), and underestimates the sub-100 nm fraction. The specific surface area measured by laser scattering, assuming LFP spherical particles with a skeletal density of 3570 kg m^{-3}, is 15 m^2 g^{-1}, which underestimates the value measured by N_2 physisorption (average 23 m^2 g^{-1}, BET). Moreover, particle shape changes as a function of the particle size. Wet media milling attrits primary particles smaller than 50 nm to spherical shapes (TEM), while the others remain as an elongated prisms, in which one dimension is twice the others (SEM: sphericity 0.8, aspect ratio 0.5). On the other hand, spray dried secondary particles are spherical or doughnut-shaped, and the mean diameter lies between 5 µm to 50 µm depending on the spray drying conditions (Figure 2b, Table 1, ESI Figure 2S). Spherical particles are preferred as they are denser, but a synergistic effect between excessive drying rate and slurry viscosity, creates doughnut holes in the higher-tail of the PSD (Figure 3j).[22] PVA increases the mixture viscosity by a factor of 4 and the secondary particle size, produces more blowholes, but decreases density. A binderless suspension yields a powder (LFP-neat) with ρ_t = 1120(10) kg m^{-3}; the LFP-lactose powder (LFP-L) reaches ρ_t = 1140(10) kg m^{-3}; while adding PVA (LFP-LP and LFP-LPU): ρ_t = 1070(50) kg m^{-3} ($CI^{95\,\%}_{n=3}$). The organic binders fill the nano and mesopore fraction of the powder (porosimetry), as result, LFP-L should be denser than LFP-neat (calc: 1200 kg m^{-3}). The two powders have similar PSD and we attribute the inconsistency to blowholes. This macroporosity averages 2 µm to 50 µm (SEM) and reduces drastically the macroscopic density of the powder (ρ_t), but not the microscopic packing efficiency of the primary particles. In fact, from porosimetry, the apparent particle density ρ_p is much higher, as we measure only pores up to 0.3 µm in diameter. LFP-neat has ρ_p = 1820(30) kg m^{-3}; LFP-L ρ_p = 2130 kg m^{-3}; LFP-LP ρ_p = 2020 kg m^{-3}; LFP-LPU ρ_p = 2110 kg m^{-3}; and the density increases coherently with the addition of binders (calc: 2000 kg m^{-3} to 2100 kg m^{-3}). This measure gives a better estimate regarding how the primary particles pack together and suggests strategies to improve the energy density of the cathode: by re-milling the

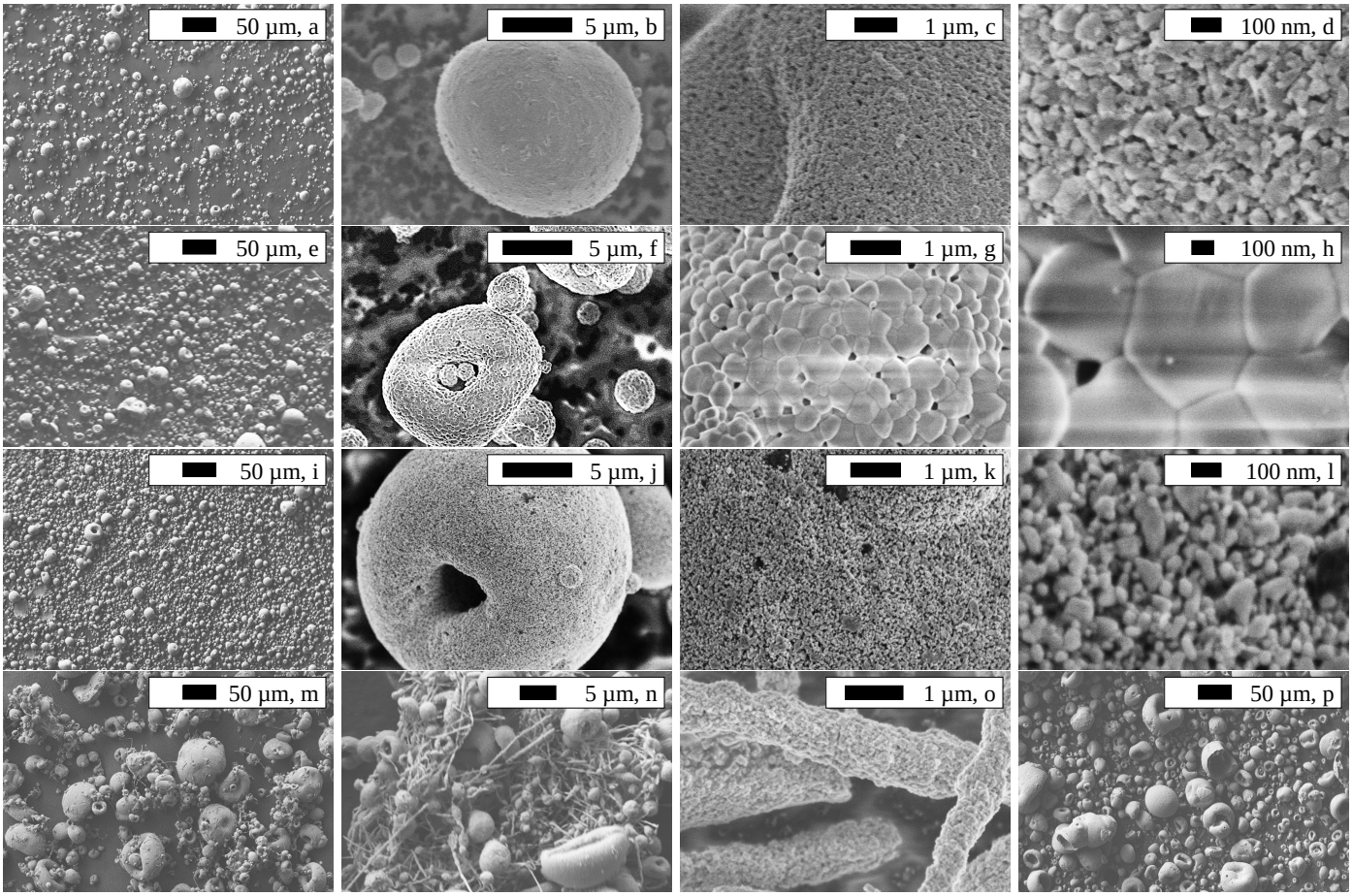

Figure 3: Particle morphology by SEM: "a" to "d" belong to the spray dried neat LFP suspension (adding lactose does not change the texture). However, calcination of LFP powders without carbon precursor sinters the primary particles together "g" and "h", but not the secondary: "e" and "f". Lactose prevents sintering and the powder remains nanostructured: "i" to l". Adding PVA changes the morphology of the spray dried material, creating submicron rods: "m" to "o". Calcination of this material breaks some particles, revealing that they are hollow "p".

calcined powder to compact the blowholes (this work) or scaling spray-drying to achieve a slower drying-rate and avoid their formation. The structure of spherical, dense particles is unaffected by calcination; while particles with blowholes, which are mechanically less resistant, break during calcination and expose their internal voidage (Figure 3p).

3.3. Pyrolysis and carbon layer

Spray drying coats homogeneously the primary particles with the carbon precursors (lactose and PVA), even inside the secondary particles. As the water recedes from the drying droplet, the capillary forces push the solvent, saturated with the carbon precursors, inside the pores of the forming secondary particles (also confirmed by a decrease in pore volume from N_2 physisorption porosimetry, Table 1). The primary particles, on the outer shell of the secondary particles, have a thinner coating vs. the bulk, as we see from TEM images of the spray dried material. However, the carbon precursors' morphology before calcination looks identical, like an amorphous nanometric coating that surrounds the primary particles and fills the interparticle voids, regardless of the type of carbon precursor added or ultrasonication (LFP-L, LFP-LP, LFP-LPU: ESI Figure 3S-5S). The presence of the carbon precursors' coating blurs the TEM images from the bulk of the material. In contrast, the neat LFP powder, with no carbon, has a better defined primary particles' contours and sharper edges (LFP-neat: ESI Figure 6S). Calcination pyrolyzes lactose into a 1 nm to 3 nm layer of semi-graphitic carbon

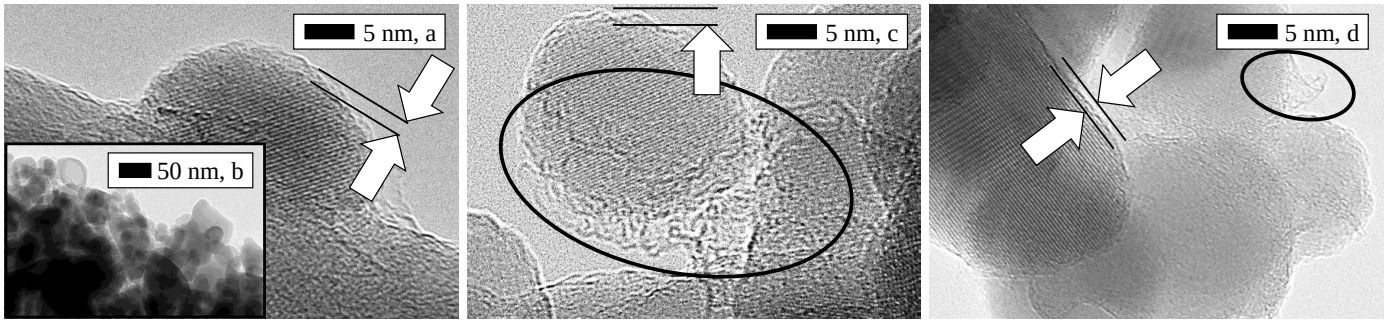

Figure 4: Carbon coat morphology by TEM after pyrolysis: lactose decomposes into a thin layer of semi-graphitic carbon (arrows, 1 nm to 3 nm, "a"), coating the primary LFP particles "b". The addition of PVA superimposes over the thin layer of lactose a grid-like carbon structure interconnecting the primary particles (circled, "c"). Ultrasonication depolymerizes PVA into a short-chain polymer so the carbon grid is now smaller—"d".

and evenly redistributes the carbon on the surface of the material, by partial gasification and condensation (Figure 4a). The carbon thickness of the surface and the bulk of the secondary particles were the same (LFP-L-Py: ESI Figure 7S, Figure 4b). However, a long polymeric chain PVA adds a new morphology after calcination: a cage, reticular grid-like carbon that connects several primary particles, covering pores voids up to 100 nm diameter (LFP-LP-Py: ESI Figure 8S, Figure 4c). Ultrasonication breaks the PVA's polymeric chain and the grid-like carbon appears smaller, between 5 nm to 20 nm in size (LFP-LPU-Py: ESI Figure 9S, Figure 4d). The surfactant Tween-20, lactose monohydrate and PVA are the three sources of carbon that coat the primary particles. Respectively, with a stoichiometric mass ratio ν_i: 57 %, 40 %, 55 % of carbon, and their contribution is linear with the amount used (ω_i: g_i/g_{LFP}; Eq. 1a).

$$\begin{aligned} C_{\text{spray dried}} &= \sum \nu_i \omega_i \\ C_{\text{pyrolyzed}} &= \sum \nu_i \omega_i \beta_i \end{aligned} \tag{1}$$

The sample variability is comparable to the regression ($C_{\text{spray dried}}$: g_{carbon}/g_{powder}): five random samples have been repeated three times, giving an average $\pm 0.1\,\%$ $CI_{n=3}^{95\,\%}$ and a relative error between 1 % to 5 %. While the linear regression has a standard error of the mean of $\pm 0.2\,\%$ with an $R^2 = 99\,\%$ (ESI Figure 10S). During pyrolysis part of the carbon oxidizes to CO and CO_2: excluding the direct reaction with gaseous oxygen, carbon at 700 °C reacts with steam (water-gas reaction). The carbon precursors' hydroxyl groups dehydrate, cyclize the molecule, and form unsaturated species, generating semi-graphitic carbon and water.[27] From a regression analysis, the β_i coefficient indicates for each component the fraction of carbon left after pyrolysis (standard error of the mean is $\pm 0.1\,\%$, R^2 >99 %, Eq. 1b). Tween-20 loses the most carbon during pyrolysis ($\beta_i = 0.15$), followed by lactose (0.52) and finally PVA (0.75).

3.4. N_2 physisorption porosimetry

A high S_a promotes greater wettability and Li^+ flow from the solid material, however, melt-synthesized LFP is intrinsically non-porous (type II isotherms).[28] Milling LFP creates nanoparticles (primary particles), and spray drying coalesces the material into a meso-macro porous spherical secondary particle. The pore network correlates to the packing efficiency of the agglomerate. The lack of a plateau over a range of high P/P_0 indicates incomplete pore filling and develop a macroporous structure, which correlates to the void fraction between secondary particles.[22] Scaling-up spray drying

from a laboratory unit (Yamato GB-22) to a pilot unit (this work) did not modify the porosity of the material. Spray dried powders, with or without binders, all exhibit a type II isotherm with a small H1 hysteresis loop in the P/P_0 0.85-0.995 range (ESI Figure 11S).[29] H1 hysteresis is often associated with agglomerates of approximately uniform spheres (the primary LFP particles).[30] While the small hysteresis' area correlates with the lack of narrow necks (ink-bottle pore shape), indicating no morphological difference in arrangements of the nanoparticles between the core and the shell of the secondary particle (homogeneous distribution).[31] Spray dried powders without binders have high specific surface area and pore volume (S_a: $28\,m^2\,g^{-1}$, V_{pore}: $0.27\,cm^3\,g^{-1}$), indicating no pore blockage in the secondary particles. While the addition of binders lowers the S_a of the powder, as the pores are gradually filled with organic precursors ($20\,m^2\,g^{-1}$, $0.2\,cm^3\,g^{-1}$, Table 1). Total V_{pore} decrease by 25 %, but pore size distribution is invariant, peaking at 45 nm, which corresponds to the average inter-primary-particle void length (blue vs. red, black and green Figure 5).

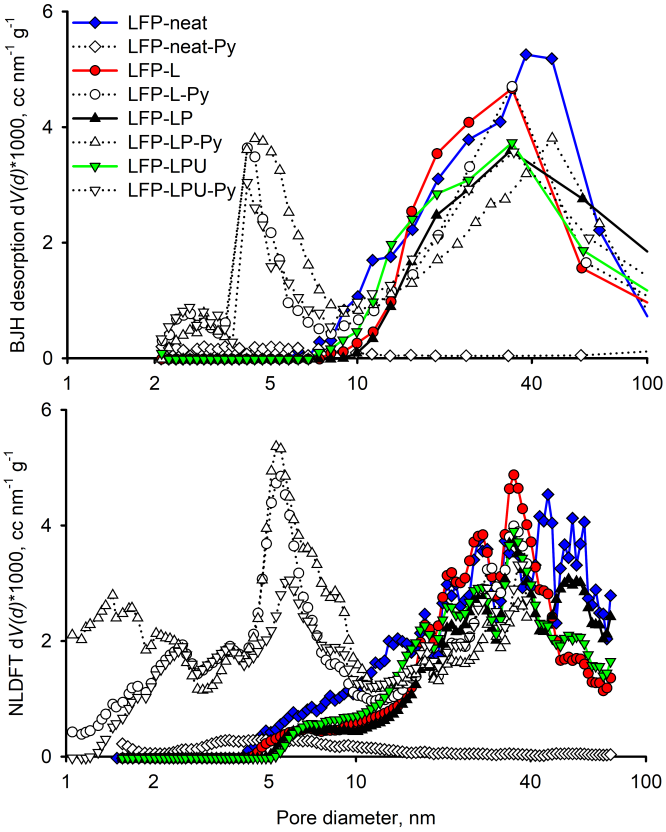

Figure 5: Comparison between BJH (top) and NLDFT (bottom) pore size distribution methods. Spray dried powders with (red, black green) or without carbon precursors (blue) shows similar pore morphology in the meso-macro pore region 5 nm to 300 nm. Calcination pyrolyzes the carbon precursors and partially sinters the LFP primary particles (open symbols).

This shows how spray drying disperses evenly the solvated organic binders over the surface of the solid LFP. In contrast, incipient wetness impregnation of a tungsten solution over a solid titania support selectively filled pores smaller than 10 nm as the tungsten loading increased.[32] Calcination imparts a radical alteration of the material. The S_a for the samples deprived or with an insufficient quantity of carbon precursor, decrease from $28\,m^2\,g^{-1}$ (before pyrolysis) to as low as $3\,m^2\,g^{-1}$ (after pyrolysis) (Table 1). Loss of S_a is seen in SEM imaging and XRD: at 700 °C the uncoated LFP nanoparticles sinter. The primary particles grow in size up to 1 µm (SEM) and XRD peaks are sharper and twice as intense. On the other hand, the samples containing the carbon precursor increase the S_a from $20\,m^2\,g^{-1}$ to $30\,m^2\,g^{-1}$ and

produce a small microporous structure (5 % to 15 % of the total S_a) and a novel pore structure between 5 nm to 10 nm (BJH and NLDFT). Accordingly, an additional H4 hysteresis loop appears between P/P_0 0.45-0.85 for the pyrolyzed powders, which is associated with the filling of micropores, in micro-mesoporous carbons; as the adsorption branch is now a composite of Types I and II isotherms (ESI Figure 11S).[31] The new narrow-mesopore structure arise from a combination of factors: calcination in the presence of carbon precursors induces partial sintering of the LFP's primary particles (XRD). The pore volume is invariant, but the pore size shifts from 45 nm (before pyrolysis, colour symbols) to 5 nm and 45 nm (after pyrolysis, open symbols, Figure 5). In the absence of carbon (diamonds) the material extensively sinters, the secondary particle shrinks (SEM), and the V_{pore} drops to 0.06 $cm^3\,g^{-1}$. Lactose and PVA maximize the micropore V_{pore} and S_a (upward triangles: 5.2 $m^2\,g^{-1}$ with the $V-t$ method, and 9.0 $m^2\,g^{-1}$ by NLDFT); lactose alone does not create a substantial microporosity (circles: 0.7 $m^2\,g^{-1}$, and 2.5 $m^2\,g^{-1}$); while ultrasonication degrades the carbon precursors (downward triangles: 0.8 $m^2\,g^{-1}$, and 0.9 $m^2\,g^{-1}$). To explain the difference in microporosity we propose that lactose coats evenly the LFP primary particles, pyrolysis decrease the thickness of the coating layer (from 6 nm to 3 nm based on a mass balance),[33] which keeps adhering to the LFP surface (TEM). The thinner carbon layer exposes a gap that ranges in the micropore region. PVA creates a carbon grid that extends between nanoparticles, ranging between 30 nm to 100 nm (TEM), which correlates with the decrease in mesoporosity (open symbols, upward triangle Figure 5). Instead, the carbon grid filament measures 1.1(1) nm in thickness (TEM), and indicates the presence of narrow CN, catalyzed on the surface of LFP.[34] Single-wall CN have a thin diameter (1.35 nm),[35] and would explain the increased N_2 adsorption in the micropore region (1.4 nm average pore volume by NLDFT); however, their characteristic peaks are absent in the Raman spectra. Hydrothermal synthesis of $LiFePO_4$ with adenosine triphosphate and ascorbic acid, creates a similar mesoporous carbon nanowire that interconnects the $LiFePO_4$ nanosheet.[36] Ultrasonication decomposes PVA and the pore size distribution follows the same trend as the sample with lactose.

3.5. Rheology of the nanoparticles suspension

The LFP suspension with Tween-20 surfactant exhibit a Newtonian rheology when the solid mass fraction is less than 20 %. Increasing solid loadings shifts it to a shear-thinning non-Newtonian fluid behavior (Figure 6).

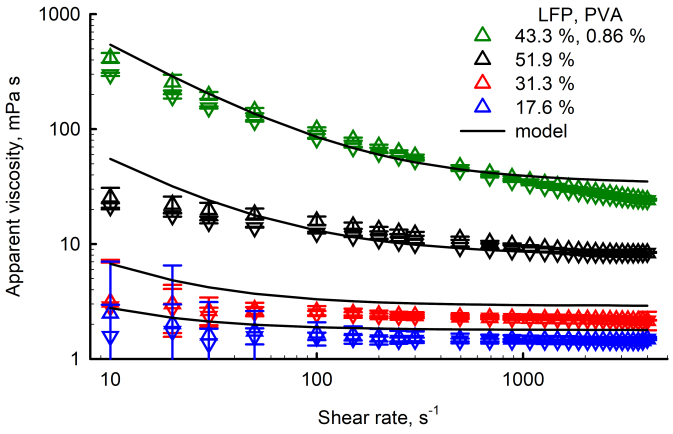

Figure 6: The shear increasing isotherms at 25.0 °C (upward triangles) on top of the shear decreasing curves (downward triangles). Viscosity increases with the solid mass fraction of LFP in water (blue, red, black). The addition of less than 7 % lactose does not modify the rheology of the material; while PVA increases the viscosity of the slurry (green). Error bars for a $CI^{95\,\%}_{n=3}$.

Dynamic apparent viscosity (μ, Pa s) decreases with shear rate ($\dot{\gamma}_{sr}$, s^{-1}) and the Herschel-Bulkley model fits best the data (R^2 >99.5 %):[37]

$$\mu = \tau_0/\dot{\gamma} + K\dot{\gamma}^{n-1} \tag{2}$$

Eq. 2 characterizes fluids with suspended solid, even in Newtonian conditions, and requires three rheometric parameters: consistency (K, Pas^n relates to the apparent viscosity), flow index (n, a measure of shear-thinning) and yield stress (τ_0, Pa). When $\tau < \tau_0$ the material behaves as a solid (τ_0 = 2 Pa to 3 Pa), and occurs when the solid mass fraction of LFP is above 60 % or at 50 % along with binders (>3 % lactose or >0.8 % PVA). In those conditions, the Tween-20 surfactant fails to maintain the LFP nanoparticles suspended and after standing still for a few hours, the material reticulates into a bulk solid with the consistency of yogurt (i.e. τ_0 = 10 Pa at room temperature). The process is reversible, indicating that the nanoparticles create a network through sol-gel physical bonds.[38] The network deforms elastically when stress is applied, via direct contact between particles. When the applied stress reaches τ_0, the network breaks up, beyond which point the suspension flows viscously.[39] Shear increasing-decreasing curves also show this thixotropic behavior. The shear increasing curve has greater viscosity, and as the analysis progresses, more energy is transferred to the material, breaking more bonds and lowering the apparent viscosity during the shear decreasing isotherm. The two curves have a hysteresis area that is maximum when the material has more suspended solids and in the presence of PVA binder (ω_{LFP} = 43.3 % with ω_{PVA} = 0.86 %: Δ_{hyst} = 10 000 Pa s^{-1}, n = 0.68). Below the mentioned conditions, Δ_{hyst} decreases proportionally with the solid mass fraction (at ω_{LFP} = 51.9 %: Δ_{hyst} = 3000 Pa s^{-1}, n = 0.81; ω_{LFP} = 35.6 %: Δ_{hyst} = 700 Pa s^{-1}, n = 0.91 and ω_{LFP} = 17.6 %: Δ_{hyst} = 100 Pa s^{-1}, n = 0.98). Also the viscosity index follows the same trend, reaching Newtonian flow (n = 1) in dilute, binder-less conditions. PVA contributes in creating a sol-gel network among LFP nanoparticles, probably by physical bonds via the PVA hydroxyl functional groups and not by dehydration reaction as the rheology is again reversible during consecutive shear increasing-decreasing isotherms and we are in the presence of an aqueous system weakly alkaline (pH 8).[32] PVA which is detrimental when spray-drying as viscosity increases and requires more energy for atomization, but is favorable when testing the electrochemistry of the material, as the PVA network pyrolyzes into a better electron conductive cage. Temperature reduces the apparent viscosity of the suspension with an exponential trend in a $1/T$ plot; solid loading, binders or different shear rates modify the magnitude of the effect but not the trend (Table 2).

At −8.9 °C an ω_{LFP} = 51.9 % binder-less suspension freezes. The process is not reversible, after thawing the material is 70 % more viscous over the entire range of temperature. PSD scattering reveals that 20 % of the solid nanomaterial agglomerates into 2 µm to 10 µm particles. Ultrasonication breaks the agglomerates and restore the original PSD and rheology. Since the change in apparent viscosity between the shear increasing and decreasing branches is negligible, we modelled the data considering four factors: LFP and PVA mass fraction, temperature and the increasing branch of the shear rate (Eq. 3).

Table 2: Rheology of LFP suspensions; the apparent viscosity (μ, ± 0.05 mPa s) increases with: increasing solid mass fraction (ω_{LFP}), or increasing PVA binder content (ω_{PVA}). While μ decreases when temperature (T) increases, or increasing shear rates ($\dot{\gamma}_{sr}$). "US": ultrasonicated suspension.

ω_{LFP} $\mathrm{g_{LFP}/g_{total}}$	ω_{PVA} $\mathrm{g_{PVA}/g_{total}}$	T °C	$\dot{\gamma}_{sr}$ $\mathrm{s^{-1}}$	μ mPa s
17.6	0	25.0	4000	1.5
31.3	0	25.0	4000	2.3
35.6	0	25.0	4000	5.2
51.9	0	45.0	4000	6.3
51.9	0	25.0	4000	8.4
60.2	0	25.0	4000	12.7
43.3	0.86	25.0	100	80.1
43.3	0.86	45.0	100	56.7
43.3	0.86	57.0	100	48.8
48.3	0	5.0	4000	10.5
48.3	0	25.0	4000	6.0
48.3	0	45.0	4000	4.2
48.3	0	65.0	4000	3.9
38.2	1.15	25.0	500	65.0
38.2	1.15	25.0	1500	43.4
38.2	1.15	25.0	4000	31.9
45.0	0.45	25.0	1000	22.4
45.0, US	0.45, US	25.0	1000	10.3
0	4.0	25.0	1000	31.8
0	4.0, US	25.0	1000	16.4

$$
\begin{aligned}
A &= e^{\frac{E_a}{R}\left(\frac{1}{T}-\frac{1}{293}\right)} \\
C &= 1 + c_{\mathrm{PVA}} * \omega_{\mathrm{PVA}} \\
\tau_0 &= \tau^* \left(1 + \left(c_{\mathrm{PVA}} * \omega_{\mathrm{PVA}}\right)^2\right) \left(\left(1 - \frac{\omega_{\mathrm{LFP}}}{\omega_0}\right)^{-4} - 1\right) \\
\mu &= A * \left[\frac{\tau_0}{\dot{\gamma}_{sr}} + K * C * \dot{\gamma}_{sr}^{-0.2 r_p \left(\frac{\omega_{\mathrm{LFP}}}{\omega_0}\right)^4} \left(1 - \frac{\omega_{\mathrm{LFP}}}{\omega_0}\right)^{-B\omega_0}\right]
\end{aligned}
\tag{3}
$$

A modified Arrhenius type relationship (A term) explains the temperature variation (T, K) for the apparent viscosity (μ, Pa s): at 20 °C $A = 1$; when $T = 5$ °C $A = 1.4$ and when $T = 70$ °C $A = 0.4$; the E_{a} regress to 16 300(500) J mol^{-1} (standard error). Interestingly, the regressed trend overlaps with the viscosity variation of pure water (in mPa s) and the regressed E_{a} agrees with previous studies for pure water ($n = 7$, 15 800(200) J mol^{-1}, standard error).[40, 41] When comparing our regressed data with another regression where we imposed the E_{a} of pure water, the Mann-Whitney U Statistic determined no statistically significant difference between the two groups ($p = 0.934$). We can therefore infer that temperature only affects the rheology of the solvent, and not the solid or interfacial property of the suspended $LiFePO_4$ nanoparticles. The PVA mass fraction linearly correlates with the consistency index K (C term) and quadratically with the yield stress τ_0, for slurries up to 0.04 ω_{PVA} ($\mathrm{g_{PVA}/g_{total}}$).[42] The quadratic function best fit the liquid-to-solid transition of our feed material when it contains PVA, the constant is set to 1 to impose neutrality for a binderless suspension, while the proportionality coefficient c_{PVA} regress to 700. The yield stress (τ_0, Pa) increases with increasing particle volume fraction (φ, L L^{-1}) with a Maron-Pierce relationship and τ^* is a fitting parameter which correlates to the solid particle size.[39] When we regressed the same equation using mass fractions we obtained $\tau^* = 0.006$ Pa and $\omega_0 = 0.77$ which

represents the maximum (mass) packing fraction. The remaining re-elaboration of the Herschel-Bulkley model include an empirical formula for evaluating the Newtonian index, as it depends systematically on particle aspect ratio (in our case $r_p = 0.5$) and solid loading.[43] The same rheological study on suspended particles regressed the Einstein coefficient B as a function of r_p (in our case $B = 2.5$) and we decided to apply the Krieger equation,[44] as a modification formula, to include a concentrated regime flow, for the consistency index K. With the Krieger modification, $K = 1.2 \times 10^{-3}\,\mathrm{Pas^n}$ regress to the viscosity of the solvent (water at 20 °C is 1 mPa s), and our regression improves: R^2 and adjusted R^2 scores are equal; R^2 passes from 99.3 % to 99.9 %; and the standard error of the estimate: from 10.0 mPa s to 4.5 mPa s (ESI Figure 12S). Converting solid mass fractions to volume fractions, and writing Eq. 3 in terms of volume fraction, does not fit the data with respect to shear increase and solid loading. ($R^2 = 99.6$ % and standard error of the estimate: 7.7 mPa s). When regressing using volume fractions, $E_a = 14\,300(900)\,\mathrm{J\,mol^{-1}}$, $\tau^* = 0.25\,\mathrm{Pa}$, $K = 0.0030\,\mathrm{Pas^n}$, $\varphi_0 = 0.66$ and $c_{PVA} = 370$. The maximum (volumetric) packing fraction is in agreement with experimental data on micron-sized particles but the yield stress fitting parameter diverges from the proposed trend: for 50 µm particles, τ^* measured 0.05 Pa; and for 2.5 µm, τ^* measured 3 Pa.[43] We extend the study into the submicron region with a broad distribution of primary particle sizes and obtain $\tau^* = 0.25\,\mathrm{Pa}$, indicating that nanoparticles act as viscosity reducers, as already demonstrated in crude oil rheology studies.[45] We also conducted a thixotropy study of a 50 % solid slurry. When shear is applied, $\dot{\gamma}_{sr}$ from $0\,\mathrm{s^{-1}}$ to $50\,\mathrm{s^{-1}}$, it takes an average of 2.5 s to reach 95 % of the steady state measured stress. Continuing from $50\,\mathrm{s^{-1}}$ to $500\,\mathrm{s^{-1}}$ it takes 1.3 s; $500\,\mathrm{s^{-1}}$ to $5000\,\mathrm{s^{-1}}$ 0.9 s; while $5000\,\mathrm{s^{-1}}$ to $500\,\mathrm{s^{-1}}$ 1.5 s; $500\,\mathrm{s^{-1}}$ to $50\,\mathrm{s^{-1}}$ 3 s; $50\,\mathrm{s^{-1}}$ to $0\,\mathrm{s^{-1}}$ 10 s. Imposing different temperatures (−5 °C to 65 °C) does not influence thixotropy, as there is no statistical difference between the temperature groups ($p = 0.998$). This effect has to be taken into consideration as the slurry that undergoes atomization is subject to a rheology different from the expected one. Feeding $100\,\mathrm{mL\,min^{-1}}$ of slurry from the tank through the pipe imposes a shear of $500\,\mathrm{s^{-1}}$, and given the dimension of the apparatus, a contact time of 10 s. The pipe is then connected to the nozzle attachment, a steel duct in which the slurry passes at $\dot{\gamma}_{sr} = 100\,\mathrm{s^{-1}}$ for 7 s. Finally the nozzle reduces the cross-section to a 0.7 mm bore, where the slurry shear at $50\,000\,\mathrm{s^{-1}}$ for 2 ms. This final sudden change in diameter (and shear rate) is unlikely to impose any actual decrease in the apparent viscosity. The thixotropy of the feed material imposes a kinetic limitation for the apparent viscosity variation due to shear and the short contact time for both the atomizer and the droplet drying (a few ms) leaves the material behaving in the $100\,\mathrm{s^{-1}}$ shear range.

3.6. Ultrasonication

In water, long chain PVA organizes to a pseudo-micelle conformation around the nanoparticles. This increases the hydrodynamic radius and thus the intrinsic viscosity of the medium.[46] In fact, adding 0.45 % PVA to a suspension of 45 % LFP increases the apparent viscosity 4-fold with respect to a binderless slurry. However, when ultrasound (US) is applied to a suspension containing PVA, the apparent viscosity drops 2-fold, permanently (Table 2). The LFP primary particle size distribution remains unchanged (before US: 130(60) nm vs. after US: 120(50) nm, spanning from $d_{v,10}$: 70 nm, $d_{v,50}$: 110 nm, to $d_{v,90}$: 190 nm). So, we attributed this effect to the depolimerization of PVA; in fact, applying US to a 4.0 % PVA solution in water, registered a 2-fold drop in viscosity. Ultrasonication degradates organics and polymers via a macro-radical mechanism,[47, 48] and depolymerizes aqueous solutions of PVA, as cavitation and macro-turbulence induce shear

forces that break the polymer's chemical bonds.[49, 50] The Mark—Houwink equation characterizes the intrinsic viscosity of a polymer with its molecular weight, while the Solomon—Ciuta equation estimates the intrinsic viscosity from single-concentration apparent viscosity measurement.[51] The 4.0 % PVA solution has an apparent viscosity of 32.0(8) mPa s at 25 °C, a Newtonian behavior, and an average molecular weight of Mw = 170 000 g mol^{-1} (manufacturer specifications). US depolymerizes the 4.0 % PVA solution to a 90 000 g mol^{-1} polymer, halving the chain length (μ = 16.8(2) mPa s). With 45 % LFP and 0.45 % PVA, the effect of US is even more pronounced. Lower polymer concentrations lead to higher polymer degradation because the polymer chains are less overlapped.[52] As a result, viscosity decreases from 22 mPa s to 10 mPa s at $\dot{\gamma}_{sr}$ = 1000 s^{-1}. Assuming both the LFP suspension and PVA contribute to the final viscosity in an additive way, a 45 % LFP suspension has a μ = 6 mPa s. Subtracting the LFP contribution from the LFP+PVA suspension, the PVA drops in viscosity 4-fold after US (16 mPa s to 4 mPa s), which corresponds to a 30 000 g mol^{-1} low molecular weight polymer.

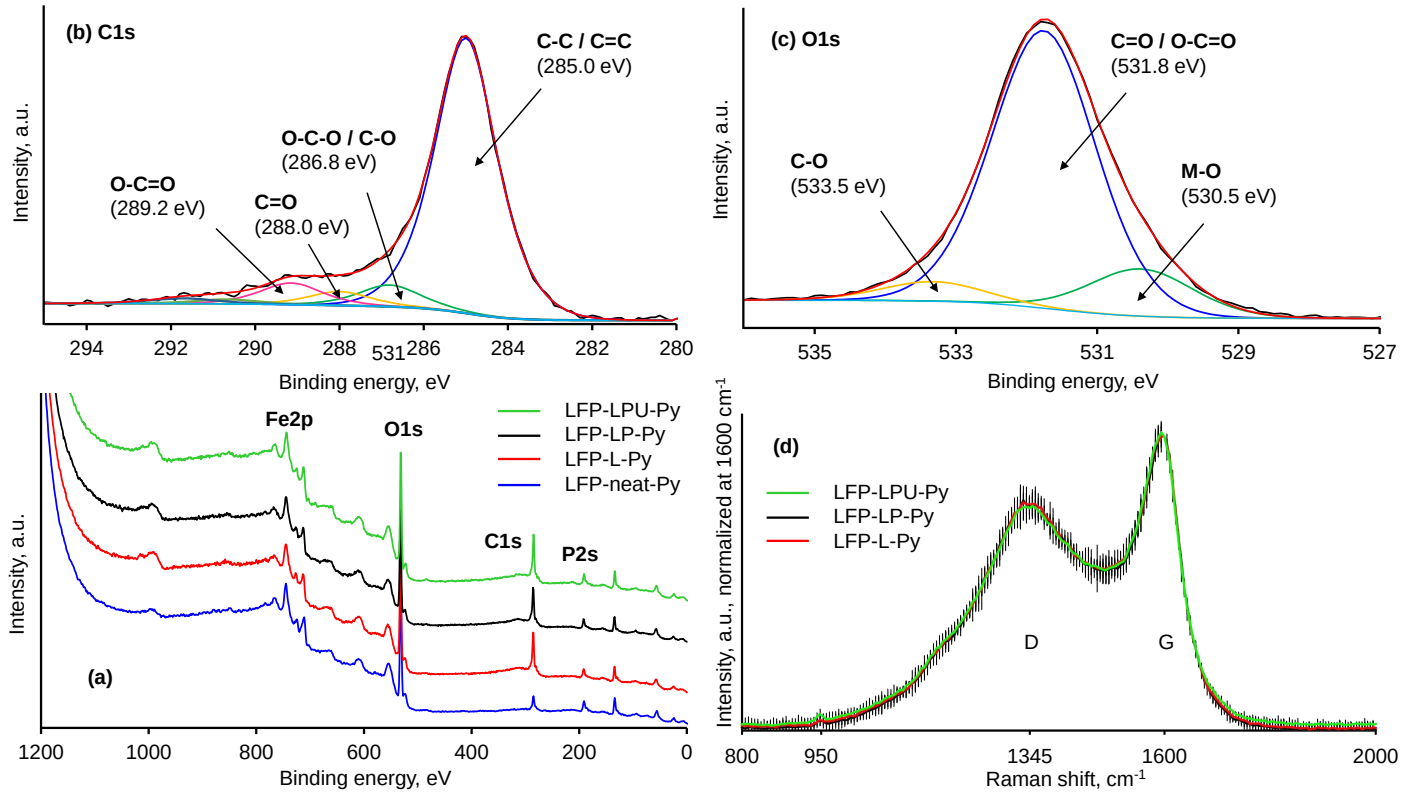

Figure 7: (a) XPS spectra for the different carbon coating and control sample, and high resolution spectra of C1s (b) and O1s (c) for LFP-LP-Py. (d) Raman spectra, the vertical bars are the $CI_{n=3}^{95\,\%}$ for each material. The small peak at 950 cm^{-1} correlates with the stretching modes of PO_4^{3-} (Full range ESI Figure 13S).

3.7. Carbon coat chemical analysis

X-ray photoelectron spectroscopy (XPS) is a surface sensitive technique that determines the chemical composition in atomic percentages of the elements and the amount of carbon–carbon/carbon–oxygen bonding (Table 3).

We investigated the effect of different carbon precursor coating on the LFP base material compared to the calcined control sample (LFP-neat-Py) by high resolution deconvolution of the C1s and O1s spectra. The XPS survey of the control and pyrolyzed samples containing lactose (LFP-L-Py), lactose-PVA (LFP-LP-Py), and ultrasonicated lactose-

Table 3: XPS elemental composition (at. ±0.2 %).

Sample	P2p	C1s	O1s	Fe2p
LFP-L-Py	7.5	41.5	46.6	4.4
LFP-LP-Py	8.4	39.8	46.3	5.4
LFP-LPU-Py	6.9	45.5	42.8	4.9
LFP-neat-Py	12.4	20.0	59.6	8.0

PVA (LFP-LPU-Py) clearly shows the elemental peaks of P, C, O and Fe, respectively (Figure 7a). Due to the presence of iron, the only lithium (Li1s) peak cannot be quantified, as they overlap. The Fe2p signal has a sensitivity factor over ten times greater than Li1s, also compared to peak intensity of carbon, lithium provides a very low sensitivity, approximately 1/18 that of carbon.[53] The calibration of all the samples peaks referred to the C1s species, corresponding to the adventitious carbon from the XPS instrument. In LFP-LP-Py, deconvoluting the C1s signal (Figure 7b) yields four peaks, the binding energy at 285.0 eV (C−C/C=O) assigned to aliphatic and aromatic structures, 286.8 eV (C−O−C/C−O) ascribed to epoxy carbon and hydroxyl carbon, 288.0 eV (C=O) corresponds to carbonyl carbon and 289.2 eV (O−C=O) represent carboxylate carbon.[54] Figure 7c shows the O1s core level spectrum: the binding energy at 530.5 eV (M−O) is characteristic of the "O^{2-} (O_I)" ions of the crystalline network bonded to a metal,[55] indicating Fe−O shear the orbital O1s in $LiFePO_4$ linkage. The characteristic peak at 531.8 eV (C=O/O−C=O) is attributed to the superoxide anions "O^{-} (O_{II})" and the peak at 533.5 eV (C−O) represent the superoxide anion "O^{2-} (O_{III})".[56] Comparing the high resolution spectra (ESI Figure 14S) and the atomic percentages (at. %) of the samples illustrated in Table 4 showed a higher proportion of C−O groups in the lactose sample, compared to lactose-PVA and the ultrasonicated one.

Table 4: Identification of functional groups and their at. % obtained from high resolution XPS spectra, fitting of the C1s (top) and O1s peaks (bottom). Raman intensity ratio between carbon's D and G bands (bottom, last column).

Sample (C1s)	C−C/C=C	C−O/C−O−C	C=O	O−C=O
LFP-L-Py	36.9	4.6	1.2	3.2
LFP-LP-Py	37.6	3.0	1.9	3.0
LFP-LPU-Py	36.8	3.3	1.9	2.7
LFP-neat-Py	18.1	1.1	–	1.7
Sample (O1s)	M−O	C=O/O−C=O	C−O	I_D/I_G
LFP-L-Py	7.2	40.7	4.5	0.77(3)
LFP-LP-Py	7.3	42.9	3.0	0.76(1)
LFP-LPU-Py	7.8	42.7	3.4	0.76(3)
LFP-neat-Py	13.0	64.4	1.7	

Similarly, a higher proportion of metal oxides is detected in the ultrasonicated sample compared to lactose and lactose-PVA samples. Instead, the at. % of the functional groups C−C/C=C is higher in the lactose-PVA powder compared to the other two. No other significant differences between the carbon and oxygen high resolution spectra could be observed in the coated samples. In comparison, the control sample LFP-neat-Py consist of very low at. % of aliphatic, aromatic and epoxy carbon, in addition no presence of carbonyl carbon, which justifies the uncoated behavior of the control sample (low percentages of C−O linkages are due to the presence of adventitious carbon). Instead, the control sample shows high percentages of metal bonding (M−O) due to the interaction of metal with oxygen in the $LiFePO_4$ base compound; this justifies that the interaction between oxygen and carbon been created by addition of the carbon precursors and the carbon coat adheres chemically with the $LiFePO_4$. We further investigated the $LiFePO_4$/C powders by calculating the intensity

ratio between the D and G bands of carbon with Raman spectroscopy (I_D/I_G) (Figure 7d). The D band (1345 cm^{-1}) is associated with out of plane vibrations: disordered sp^3 tetrahedral amorphous carbon. The G band (1600 cm^{-1}) correlates to in-plane vibrations: graphitic sp^2 carbon.[57] The three samples' spectra overlap with no statistical differences, and the I_D/I_G is as-well invariant (one-way ANOVA test, $p = 0.49$, Tab. 4). This further confirms that the carbon coating is chemically equivalent and differs only in terms of morphology between the three main samples (carbon-grid, TEM).

3.8. Electrochemical tests

At the beginning, we run preliminary tests to identify how the spray drying conditions, secondary particle size and carbon content affect the discharge capacity (ESI Table 1S). Small particles, with a narrow size distribution, are more stable during cycling (by linearly extrapolating the trend between the 30^{th} to 45^{th} cycle). The spray dried LFP powder with lactose, with a $D_{4,3}$ diameter of 7(3) µm (distribution at one standard deviation) is stable after 15 cycles (red circles, ESI Figure 15S). The samples reach the maximum capacity after several activation cycles, which is normal. The activation is related to pulverization due to the presence of a thicker carbon coating (present inside the interparticle void fraction: TEM and N_2 physisorption porosimetry) or large particle agglomerates. By cracking these agglomerates, new active surfaces become accessible. This effect is modest, improving 1 % of the battery's capacity, indicating that the primary particles are already well dispersed and the carbon coat has an uniform thickness with lactose. Increasing the secondary particle diameter to 12(10) µm (yellow diamonds, ESI), broadens the distribution and the cyclability rate drops twice as fast with respect to the previous material. PVA increases the viscosity of the slurry, and the size of the particles (32(23) µm). The discharge capacity drops sooner and one battery fails, due to incomplete and uneven carbon coverage and probably mechanical detachment of the material (black upwards triangles, ESI). On the other hand, adding lactose and PVA, maintains both batteries active and relatively stable, despite the larger particle size: 32(21) µm (green downwards triangles, ESI). Therefore, we optimized the spray drying conditions to deliver a fine powder ($D_{4,3} = 10$ µm). Spray drying the suspension without binders and calcination, produce a material with poor electrochemical capacity (due to the lack of a carbon coat and sintering) but stable cyclability (yellow squares, Figure 8a).

Subsequently, we optimized the binder formulation, aiming for a 3 % carbon coating after pyrolysis. During spray drying with binders, to compensate for the LFP suspension's higher viscosity, we increased the atomization pressure to 0.40 MPa and obtained particles with a mode below 12 µm. We prepared three powders with similar characteristics after pyrolysis, in terms of: carbon content, secondary particle size and S_a (Table 1). For the first, we spray dried a suspension of LFP with 14.5 % lactose (mass basis on dry LFP, LFP-L-Py, red circles). Then 11 % lactose and 1 % PVA (LFP-LP-Py, black upward triangles). While the third sample contained 11 % lactose, 1 % PVA and was ultrasonicated before and during spray drying (LFP-LPU-Py, green downward triangles), to compare the role of US as dispersing force. All materials are initially cycled at 0.1C for 10 cycles (not shown) and have a rapid activation, reaching the maximum capacity after 6 cycles. During the first 100 cycles at 1C, the materials behave similarly, with no statistical differences (ANOVA on ranks test, $p = 0.33$). After, however, the lactose-based material's discharge capacity quickly fades due to polarization of the cathode, while the lactose-PVA materials remain constant. This supports the hypothesis that the carbon-cage helps to dissipate the charge and maintains the nanoparticles cohesive, thus improving the cathode's cyclability. We

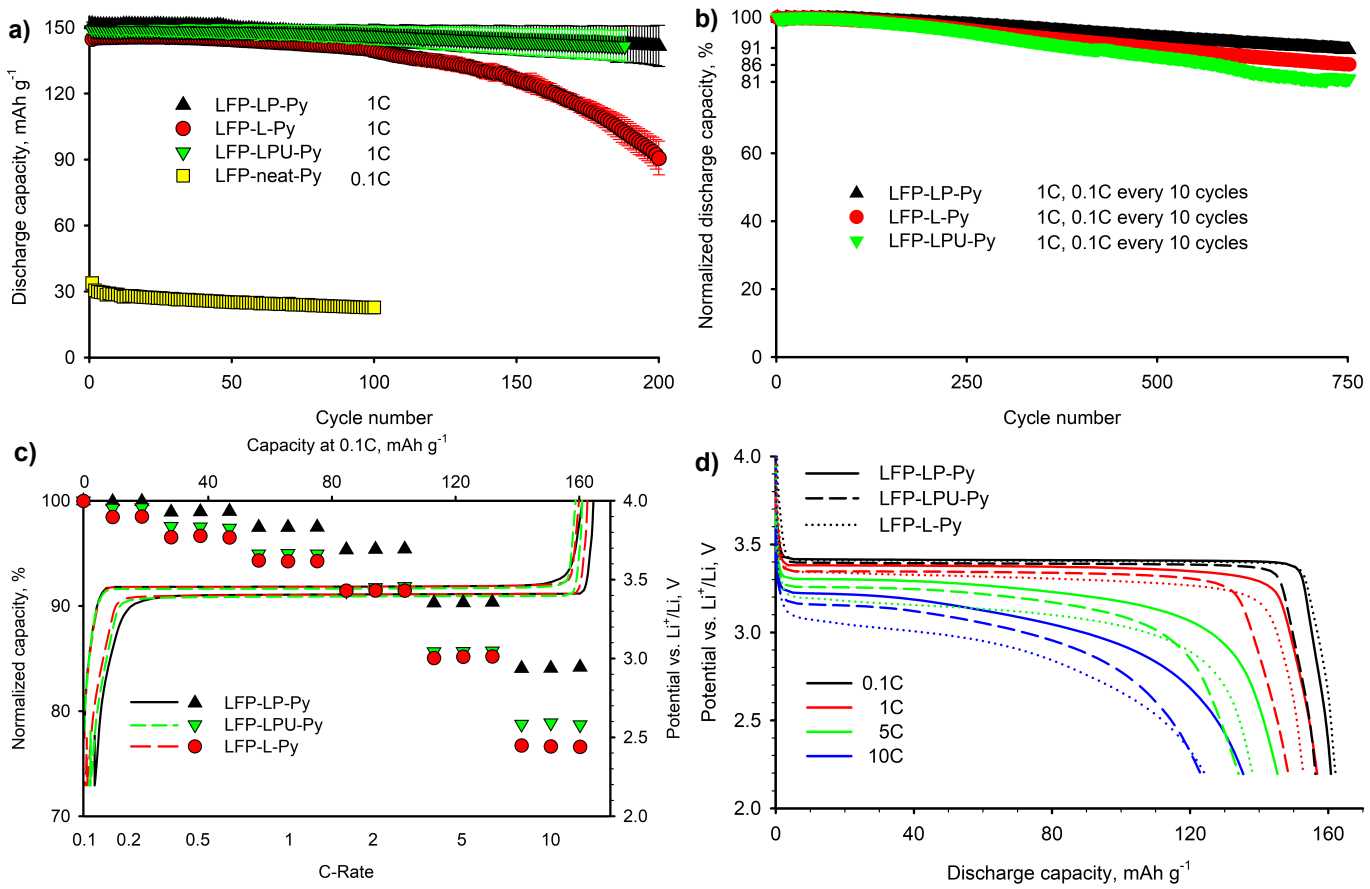

Figure 8: a) Cyclability at 1C discharge rate and 0.1C for the neat LFP. Error bars represent 1 standard deviation, $n = 2$. Adding PVA significantly improves the cyclability of the battery vs. the lactose based material ($p < 0.02$). b) Normalized cyclability at 1C discharge rate (one every 10 cycles is conducted at 0.1C and not shown on the graph for simplicity). Lactose-PVA confer greater stability, the coin-cell battery would retain 80 % of the initial capacity after 1700 cycles (vs. lactose: 1100 cycles). Ultrasonication shortens the PVA's chain length and induce instability in the trend. c) Rate performance (bottom-left axes, symbols) and Galvanostatic curves (top-right). The addition of high-M_w PVA (black lines and upward triangles) creates an extended carbon grid that better distributes the electric charge across the LFP nanoparticles, improving the discharge capacity. d) Discharge curves at increasing C-rates. An extended carbon-grid (solid line) dissipates the charge more efficiently at high C-rates with respect to a shorter carbon-grid (dashed) or no grid (dotted).

repeated and extended the cyclability tests over 750 cycles at 1C (Figure 8b). To avoid charge accumulation and dendrite formation, one every 10 cycles is conducted at 0.1C, this allowed the lactose-based cathode to regenerate for comparative results.[58] This methodology gives us a better understanding of the cathode's aging process, as the crystalline matrix deforms during Li^+ intercalation. This results in mechanical stress that fractures the cathode and isolate part of the nanomaterial, consequently the discharge capacity drops. At 750 cycles, LFP-LP-Py retains 91 % of the initial capacity (150.7 mA h g^{-1} at 1C). LFP-L-Py 86 % (153.7 mA h g^{-1} at 1C). Both materials decline linearly, but the carbon cage further extends cyclability by 50 % vs. the lactose-based material. LFP-LPU-Py retains 81 % (initial: 150.0 mA h g^{-1} at 1C). Despite having an even better cyclability up to 100 cycles, the material quickly deteriorates and the trend becomes unstable. The PVA's chain length after ultrasonication is shorter, and the resulting carbon-cage does not connect the nanoparticles together (TEM). We speculate that ultrasonication induces a better dispersion of the lower-end tail of the primary particle size distribution. Small nanoparticles tend to clump together into bigger, more resistant clusters. Ultrasound breaks these clusters and the spray dried powder is less resistant to mechanical stress, and ages faster. This explains the lower cyclability, but the better rate performance with respect to the lactose based material, as the carbon

cage still plays a role in dissipating the electric charge more efficiently. Galvanostatic cycling at 0.1C, for LFP-LP-Py, LFP-LPU-Py and LFP-L-Py, shows a single flat plateau at 3.4 V versus Li^+/Li, indicating the two-phase reaction between the LFP triphylite and the heterosite $FePO_4$ upon lithiation/de-lithiation reactions (Figure 8c). No extra plateau related to impurity phases was observed. A polarization of 50 mV was observed for all three samples indicating that all three samples are sufficiently well carbon coated for this cycling.[59] In the rate performance test, the capacities at different C-rate (0.1 to 10) were normalized with respect to the capacity at 0.1C (Figure 8c). The rate capabilities of the samples up to 10C are comparable to what is typically found for high performance materials.[60, 15] By increasing the C-rate, the difference in rate capability between these three samples becomes more obvious. LFP-LP-Py exhibited the highest discharge capacity of 135 $mA\,h\,g^{-1}$ at 10C (84 % normalized capacity vs. initial: 161 $mA\,h\,g^{-1}$ at 0.1C); LFP-LPU-Py 123 $mA\,h\,g^{-1}$ at 10C (79 % vs. initial: 156 $mA\,h\,g^{-1}$ at 0.1C); and LFP-L-Py 124 $mA\,h\,g^{-1}$ at 10C (77 % vs. initial: 162 $mA\,h\,g^{-1}$ at 0.1C). Considering the pyrolyzed powders contain 94.9(4) % $LiFePO_4$ active material (the rest is carbon and γ-Li_3PO_4), LFP-LP-Py reaches the maximum attainable capacity at 0.1C: 169.7(7) mAh/g($LiFePO_4$) (170 $mA\,h\,g^{-1}$ theoretical). We made sure that the three contrast samples have similar active material loading, thickness (experimental section), carbon loading and secondary particle size (Table 1) for comparative kinetic investigation. The chemical composition is also similar (XPS and Raman), thus we conclude that adding high-M_w PVA to lactose and pyrolysis produce a morphological difference in the carbon coating. A carbon-cage interconnects the primary particles (TEM) which improves even further the discharge rate and cyclability versus the lactose-based covered cathode. The powder gains microporosity as a result, which shortens the diffusion path of the Li^+ in the solvent, increasing access to the active surface area (porosimetry, Table 1). The discharge curves have flat plateau up to 1C for all materials (Figure 8d). By increasing the discharge rate up to 5C, a single plateau is still found for the lactose-PVA material (solid line). The addition of high-M_w PVA creates an extended carbon grid, interconnecting LFP primary particles, that minimizes the polarization of the cathode during discharging. While for the other two samples, the discharge curves progressively fall shorter and the plateau disappears, indicating polarization (i.e. kinetic limitation) in the materials.

4. Conclusions

Melt-synthesized LFP nanoparticles, spray dried and coated with lactose and PVA, delivers a high-performance $LiFePO_4$/C cathode material (135 $mA\,h\,g^{-1}$ at 10C). We propose an industrially scalable route, from solid state reactions, to LFP nanoparticles suspended in water. The slurry feeds a 0.8 m I.D. spray dryer, that generates 7 $kg\,h^{-1}$ of mesoporous powder, promoting Li^+ wettability and providing a homogeneous dispersion of the carbon precursors, even inside the secondary particles. A fine powder ($D_{4,3} < 12\,\mu m$) improves cyclability, but a suspension containing PVA is more viscous and spray drying requires 0.40 MPa to atomize the slurry. We model the suspension rheology, based on shear, temperature, LFP and PVA loading in water. We prove that high-M_w PVA pyrolyzes into a carbon-cage that interconnects the nanoparticles and we model the pyrolysis step, as part of the carbon gasifies. The cage forms carbon-nanopores averaging 1.4 nm in diameter, and contributes to 30 % of the S_a. The electrically conductive carbon-cage dissipates the charge more efficiently at high C-rates, and a bigger cage improves the cyclability by holding the nanoparticles together.

This reduces the mechanical stress due to lattice deformation of the LFP's crystallites during Li^+ de/intercalation, and delays the cathode's fracturing. Ultrasonication depolymerizes PVA; the resulting carbon-grid is smaller, does not interconnect the LFP nanoparticles, and induces battery failure. However, changing the acoustic frequency and amplitude, may better disperse the suspension without fragmenting the PVA chain.

Conflicts of interest

There are no conflicts to declare.

Acknowledgements

The authors recognize the support of Natural Science, Engineering Research Council of Canada and the Canadian Foundation for Innovation through the Automotive Partnership Canada program and our industrial partner Johnson-Matthey Battery Materials. The authors appreciate the collaboration of Dr. Pierre Sauriol (Polytechnique Montreal) and Dr. Delin Li, Dr. Wojciech Kasprzak, (and colleagues) of CanmetMATERIALS for generating the pilot scale melt-synthesized LFP ingots used for this study.

References

[1] J. Wang, X. Sun, Olivine $LiFePO_4$: the remaining challenges for future energy storage, Energy Environ. Sci. 8 (2015) 1110–1138. doi:10.1039/C4EE04016C.

[2] Z. P. Cano, D. Banham, S. Ye, A. Hintennach, J. Lu, M. Fowler, Z. Chen, Batteries and fuel cells for emerging electric vehicle markets, Nature Energy 3 (2018) 279–289. doi:10.1038/s41560-018-0108-1.

[3] J. B. Goodenough, M. H. Braga, Batteries for electric road vehicles, Dalton Trans. 47 (2018) 645–648. doi:10.1039/C7DT03026F.

[4] A. Varzi, D. Bresser, J. von Zamory, F. Müller, S. Passerini, $ZnFe_2O_4$−C/$LiFePO_4$−CNT: A novel high-power lithium-ion battery with excellent cycling performance, Advanced Energy Materials 4 (10) (2014) 1400054. doi:10.1002/aenm.201400054.

[5] J.-M. Tarascon, M. Armand, Issues and challenges facing rechargeable lithium batteries, Nature 414 (2001) 359. doi:10.1038/35104644.

[6] A. K. Padhi, K. S. Nanjundaswamy, C. Masquelier, S. Okada, J. B. Goodenough, Effect of structure on the Fe_3^+/Fe_2^+ redox couple in iron phosphates, Journal of The Electrochemical Society 144 (5) (1997) 1609–1613. doi:10.1149/1.1837649.

[7] J. Li, J. K. Barillas, C. Guenther, M. A. Danzer, A comparative study of state of charge estimation algorithms for $LiFePO_4$ batteries used in electric vehicles, Journal of Power Sources 230 (2013) 244–250. doi:10.1016/j.jpowsour.2012.12.057.

[8] J. Liu, Z. Wang, G. Zhang, Y. Liu, A. Yu, Size-controlled synthesis of lifepo$_4$/c composites as cathode materials for lithium ion batteries, Int. J. Electrochem. Sci. 8 (2013) 2378–2387.

[9] F. Croce, A. D'Epifanio, J. Hassoun, A. Deptula, T. Olczac, B. Scrosati, A novel concept for the synthesis of an improved $LiFePO_4$ lithium battery cathode, Electrochemical and Solid-State Letters 5 (3) (2002) A47–A50. doi:10.1149/1.1449302.

[10] A. S. Arico, P. Bruce, B. Scrosati, J. M. Tarascon, W. V. Schalkwijc, Nat. Mater. 4 (2005) 366. doi:10.1002/anie.200702505.

[11] Y. Wang, Y. Wang, E. Hosono, K. Wang, H. Zhou, The design of a $LiFePO_4$/carbon nanocomposite with a core-shell structure and its synthesis by an in situ polymerization restriction method, Angewandte Chemie International Edition 47 (39) 7461–7465. doi:10.1002/anie.200802539.

[12] M. Gauthier, M. K. Domroese, J. A. Hoffman, D. D. Lindeman, J. R. G. Noel, V. E. Radewald, J. Rouillard, R. Rouillard, T. Shiota, J. L. Trice, In-situ short circuit protection system and method for high-energy electrochemical cells, US6099986 (1997).

[13] M. Gauthier, M. Armand, K. Zaghib, S. Poirier, R. Bellemare, Alloyed and dense anode sheet with local stress relaxation, US6265099 (2001).

[14] D. Bresser, D. Buchholz, A. Moretti, A. Varzi, S. Passerini, Alternative binders for sustainable electrochemical energy storage – the transition to aqueous electrode processing and bio-derived polymers, Energy Environ. Sci. 11 (2018) 3096–3127. doi:10.1039/C8EE00640G.

[15] M. Talebi-Esfandarani, S. Rousselot, M. Gauthier, P. Sauriol, G. Liang, M. Dollé, $LiFePO_4$ synthesized via melt synthesis using low-cost iron precursors, Journal of Solid State Electrochemistry 20 (7) (2016) 1821–1829. doi:10.1007/s10008-015-3049-7.

[16] W. Kasprzak, D. Li, G. S. Patience, P. Sauriol, H. Villazon-Amaris, M. Dolle, M. Gauthier, S. Rousselot, M. Talebi-Esfandarani, T. Bibienne, X. Sun, Y. Liu, G. Liang, Using induction melting to make lithium-ion battery material, Advanced Materials & Processes 175 (8) (2017) 16–22.

[17] H. Villazon, P. Sauriol, S. Rousselot, M. Talebi-Esfandarani, T. Bibienne, M. Gauthier, G. Liang, M. Dollé, P. Chartrand, Melt-synthesis of $LiFePO_4$ over a metallic bath, The Canadian Journal of Chemical Engineering 0. doi:10.1002/cjce.23406.

[18] D. Li, W. Kasprzak, G. S. Patience, P. Sauriol, H. Villazón-Amarís, M. Dollé, M. Gauthier, S. Rousselot, M. Talebi-Esfandarani, T. Bibienne, X. Sun, Y. Liu, G. Liang, Production of lithium-ion cathode material for automotive batteries using melting casting process, in: J.-Y. Hwang, T. Jiang, M. W. Kennedy, D. Gregurek, S. Wang, B. Zhao, O. Yücel, E. Keskinkilic, J. P. Downey, Z. Peng, R. Padilla (Eds.), 9th International Symposium on High-Temperature Metallurgical Processing, Springer International Publishing, Cham, 2018, pp. 135–146.

[19] H. Li, A. Ndjamo, P. Sauriol, G. S. Patience, Optimization of $LiFePO_4$ wet media milling and regressive population balance modeling, Advanced Powder Technology 28 (3) (2017) 1000–1007. doi:http://dx.doi.org/10.1016/j.apt.2017.01.004.

[20] N. Abatzoglou, R. Gosselin, M. A. Inam, Rheological characterisation and phenomenological modelling of non-aqueous nano-suspensions of iron carbide produced by plasma spray, The Canadian Journal of Chemical Engineering 92 (1) (2014) 68–74. doi:10.1002/cjce.21859.

[21] N. Saadatkhah, M. G. Rigamonti, D. C. Boffito, H. Li, G. S. Patience, Spray dried SiO_2 WO_3/TiO_2 and SiO_2 vanadium pyrophosphate core-shell catalysts, Powder Technology 316 (Supplement C) (2017) 434–440. doi:10.1016/j.powtec.2016.10.056.

[22] M. G. Rigamonti, Y.-X. Song, H. Li, N. Saadatkhah, P. Sauriol, G. S. Patience, Influence of atomization conditions on spray drying lithium iron phosphate nanoparticle suspensions, The Canadian Journal of Chemical Engineering 97 (8) (2019) 2251–2258. doi:10.1002/cjce.23106.

[23] N. Ravet, M. Gauthier, K. Zaghib, J. Goodenough, A. Mauger, F. Gendron, C. Julien, Mechanism of the Fe^{3+} reduction at low temperature for $LiFePO_4$ synthesis from a polymeric additive, Chemistry of Materials 19 (10) (2007) 2595–2602. doi:10.1021/cm070485r.

[24] T. Satyavani, A. S. Kumar, P. S. Rao, Methods of synthesis and performance improvement of lithium iron phosphate for high rate li-ion batteries: A review, Engineering Science and Technology, an International Journal 19 (1) (2016) 178–188. doi:10.1016/j.jestch.2015.06.002.

[25] N. I. P. Ayu, E. Kartini, L. D. Prayogi, M. Faisal, Supardi, Crystal structure analysis of Li_3PO_4 powder prepared by wet chemical reaction and solid-state reaction by using x-ray diffraction (xrd), Ionics 22 (7) (2016) 1051–1057. doi:10.1007/s11581-016-1643-z.

[26] H. Li, M. Rostamizadeh, K. Mameri, D. C. Boffito, N. Saadatkhah, M. G. Rigamonti, G. S. Patience, Ultrasound assisted wet stirred media mill of high concentration $LiFePO_4$ and catalysts, The Canadian Journal of Chemical Engineeringdoi:10.1002/cjce.23212.

[27] D. Carnevali, M. G. Rigamonti, T. Tabanelli, G. S. Patience, F. Cavani, Levulinic acid upgrade to succinic acid with hydrogen peroxide, Applied Catalysis A: General 563 (2018) 98–104. doi:10.1016/j.apcata.2018.06.034.

[28] R. Bardestani, G. S. Patience, S. Kaliaguine, Experimental methods in chemical engineering: specific surface area and pore size distribution measurements—bet, bjh, and dft, The Canadian Journal of Chemical Engineering 97 (11) (2019) 2781–2791.

[29] K. S. W. Sing, D. H. Everett, R. A. W. Haul, L. Moscou, R. A. Pierotti, J. Roquerol, T. Siemieniewska, Pure Appl. Chem. 57 (1985) 603.

[30] Q. Instruments, Gas sorption system operating manual, Quantachrome Instruments, 2015.

[31] M. Thommes, K. Kaneko, A. V. Neimark, J. P. Olivier, F. Rodriguez-Reinoso, J. Rouquerol, K. S. Sing, Physisorption of gases, with special reference to the evaluation of surface area and pore size distribution (iupac technical report), Pure and Applied Chemistry 87 (2015) 1051–1069. doi:10.1515/pac-2014-1117.

[32] D. Carnevali, O. Guévremont, M. G. Rigamonti, M. Stucchi, F. Cavani, G. S. Patience, Gas-phase fructose conversion to furfural in a microfluidized bed reactor, ACS Sustainable Chemistry & Engineering 6 (4) (2018) 5580–5587. doi:10.1021/acssuschemeng.8b00510.

[33] M. Trudeau, D. Laul, R. Veillette, A. Serventi, A. Mauger, C. Julien, K. Zaghib, In situ high-resolution transmission electron microscopy synthesis observation of nanostructured carbon coated $LiFePO_4$, Journal of Power Sources 196 (18) (2011) 7383–7394. doi:10.1016/j.jpowsour.2011.04.003.

[34] W. Cheung, F. Pontoriero, O. Taratula, A. M. Chen, H. He, Dna and carbon nanotubes as medicine, Advanced Drug Delivery Reviews 62 (6) (2010) 633–649, from Biology to Materials: Engineering DNA and RNA for Drug Delivery and Nanomedicine. doi:10.1016/j.addr.2010.03.007.

[35] A. C. Torres-Dias, T. F. Cerqueira, W. Cui, M. A. Marques, S. Botti, D. Machon, M. A. Hartmann, Y. Sun, D. J. Dunstan, A. San-Miguel, From mesoscale to nanoscale mechanics in single-wall carbon nanotubes, Carbon 123 (2017) 145–150. doi:10.1016/j.carbon.2017.07.036.

[36] X. Zhang, Z. Bi, W. He, G. Yang, H. Liu, Y. Yue, Fabricating high-energy quantum dots in ultra-thin $LiFePO_4$ nanosheets using a multifunctional high-energy biomolecule-atp, Energy Environ. Sci. 7 (2014) 2285–2294. doi:10.1039/C3EE44187C.

[37] W. H. Herschel, R. Bulkley, Konsistenzmessungen von gummi-benzollösungen, Kolloid-Zeitschrift 39 (4) (1926) 291–300. doi:10.1007/BF01432034.

[38] A. R. Studart, E. Amstad, L. J. Gauckler, Colloidal stabilization of nanoparticles in concentrated suspensions, Langmuir 23 (3) (2007) 1081–1090, pMID: 17241017. doi:10.1021/la062042s.

[39] L. Heymann, S. Peukert, N. Aksel, On the solid-liquid transition of concentrated suspensions in transient shear flow, Rheologica Acta 41 (4) (2002) 307–315. doi:10.1007/s00397-002-0227-1.

[40] R. Haj-Kacem, N. Ouerfelli, J. Herráez, M. Guettari, H. Hamda, M. Dallel, Contribution to modeling the viscosity arrhenius-type equation for some solvents by statistical correlations analysis, Fluid Phase Equilibria 383 (2014) 11–20. doi:10.1016/j.fluid.2014.09.023.

[41] A. Messaâdi, N. Dhouibi, H. Hamda, F. B. M. Belgacem, Y. H. Adbelkader, N. Ouerfelli, A. H. Hamzaoui1, A new equation relating the viscosity arrhenius temperature and the activation energy for some newtonian classical solvents, Journal of Chemistry 2015 (2015) 12. doi:10.1155/2015/163262.

[42] M. Mohsen-Nia, H. Modarress, Viscometric study of aqueous poly(vinyl alcohol) (pva) solutions as a binder in adhesive formulations, Journal of Adhesion Science and Technology 20 (12) (2006) 1273–1280. doi:10.1163/156856106778456636.

[43] S. Mueller, E. W. Llewellin, H. M. Mader, The rheology of suspensions of solid particles, Proceedings of the Royal Society of London A: Mathematical, Physical and Engineering Sciences 466 (2116) (2010) 1201–1228. doi:10.1098/rspa.2009.0445.

[44] I. M. Krieger, Rheology of monodisperse latices, Advances in Colloid and Interface Science 3 (2) (1972) 111–136. doi:10.1016/0001-8686(72)80001-0.

[45] E. A. Taborda, C. A. Franco, S. H. Lopera, V. Alvarado, F. B. Cortés, Effect of nanoparticles/nanofluids on the rheology of heavy crude oil and its mobility on porous media at reservoir conditions, Fuel 184 (2016) 222–232. doi:10.1016/j.fuel.2016.07.013.

[46] B. M. Budhlall, K. Landfester, E. D. Sudol, V. L. Dimonie, A. Klein, M. S. El-Aasser, Characterization of partially hydrolyzed poly(vinyl alcohol). effect of poly(vinyl alcohol) molecular architecture on aqueous phase conformation, Macromolecules 36 (25) (2003) 9477–9484. doi:10.1021/ma030027d.

[47] M. Stucchi, A. Elfiad, M. Rigamonti, H. Khan, D. Boffito, Water treatment: Mn-tio2 synthesized by ultrasound with increased aromatics adsorption, Ultrasonics Sonochemistry 44 (2018) 272–279. doi:10.1016/j.ultsonch.2018.01.023.

[48] A. Akyüz, H. Catalgil-Giz, A. T. Giz, Kinetics of ultrasonic polymer degradation: Comparison of theoretical models with on-line data, Macromolecular Chemistry and Physics 209 (8) (2008) 801–809. doi:10.1002/macp.200700533.

[49] D. C. Boffito, E. Martinez-Guerra, V. G. Gude, G. S. Patience, Conversion of Refined and Waste Oils by Ultrasound-Assisted Heterogeneous Catalysis, Springer Singapore, Singapore, 2016, pp. 931–963. doi:10.1007/978-981-287-278-4_12.

[50] A. Grönroos, P. Pirkonen, J. Heikkinen, J. Ihalainen, H. Mursunen, H. Sekki, Ultrasonic depolymerization of aqueous polyvinyl alcohol, Ultrasonics Sonochemistry 8 (3) (2001) 259–264. doi:10.1016/S1350-4177(01)00086-4.

[51] A. V. Mohod, P. R. Gogate, Ultrasonic degradation of polymers: Effect of operating parameters and intensification using additives for carboxymethyl cellulose (cmc) and polyvinyl alcohol (pva), Ultrasonics Sonochemistry 18 (3) (2011) 727–734. doi:10.1016/j.ultsonch.2010.11.002.

[52] M. T. Taghizadeh, A. Mehrdad, Calculation of the rate constant for the ultrasonic degradation of aqueous solutions of polyvinyl alcohol by viscometry, Ultrasonics Sonochemistry 10 (6) (2003) 309–313. doi:10.1016/S1350-4177(03)00110-X.

[53] K. Tsutsumi, M. Shima, A. Tanaka, Advanced analysis of active material in li-ion battery by xps and aes, JEOL News 49 (1) (2014) 59–72.

[54] H. Khan, M. G. Rigamonti, D. C. Boffito, Enhanced photocatalytic activity of Pt-TiO_2/WO_3 hybrid material with energy storage ability, Applied Catalysis B: Environmental 252 (2019) 77–85. doi:10.1016/j.apcatb.2019.04.019.

[55] J.-C. Dupin, D. Gonbeau, P. Vinatier, A. Levasseur, Systematic xps studies of metal oxides, hydroxides and peroxides, Phys. Chem. Chem. Phys. 2 (2000) 1319–1324. doi:10.1039/A908800H.

[56] Y. Guo, C. Li, S. Lu, C. Zhao, Low temperature co catalytic oxidation and kinetic performances of KOH-hopcalite in the presence of CO_2, RSC Adv. 6 (2016) 7181–7188. doi:10.1039/C5RA23806D.

[57] X. Lou, Y. Zhang, Synthesis of $LiFePO_4$/C cathode materials with both high-rate capability and high tap density for lithium-ion batteries, J. Mater. Chem. 21 (2011) 4156–4160. doi:10.1039/C0JM03331F.

[58] N. D. Trinh, D. Lepage, D. Aymé-Perrot, A. Badia, M. Dollé, D. Rochefort, An artificial lithium protective layer that enables the use of acetonitrile-based electrolytes in lithium metal batteries, Angewandte Chemie International Edition 57 (18) (2018) 5072–5075. doi:10.1002/anie.201801737.

[59] M. Talebi-Esfandarani, S. Rousselot, M. Gauthier, P. Sauriol, M. Duttine, A. Wattiaux, Y. Liu, A. X. Sun, G. Liang, M. Dollé, Control of the $LiFePO_4$ electrochemical properties using low-cost iron precursor in a melt process, Journal of Solid State Electrochemistry 20 (9) (2016) 3481–3490.

[60] B. Wang, W. Al Abdulla, D. Wang, X. S. Zhao, A three-dimensional porous $LiFePO_4$ cathode material modified with a nitrogen-doped graphene aerogel for high-power lithium ion batteries, Energy Environ. Sci. 8 (2015) 869–875. doi:10.1039/C4EE03825H.